New Interstellar Laboratories in the Molecular Ring

Faraday Discussions

ARTICLE TYPE

New Interstellar Laboratories in the Molecular Ring[†]

Olivia H. Wilkins[*‡] and Geoffrey A. Blake

Much of what is known about chemistry in star-forming regions comes from observations of nearby ($d < 500$ pc) low-mass protostars. For chemistry in high-mass star-forming regions, several more distant ($d \sim 2-8$ kpc), exceptionally bright molecular sources have also been the subjects of repeated observations but with concomitantly poorer linear spatial resolution. Facilities such as ALMA and JWST, however, now provide the means for observing distant sources at dramatically higher spatial resolution and sensitivity. We used the modest resolving power of the Atacama Compact Array, a dedicated subset of ALMA antennas, to carry out a pilot survey of 11 giant molecular clouds selected from the Bolocam Galactic Plane Survey [Battisti & Heyer, *Astrophys. J.*, 2014, **780**, 173] within the so-called molecular ring between about 4 and 8 kpc from the galactic center. Within our observed sample, molecular emission regions—most of which correspond to at least one (candidate) young stellar object—exhibit a range of chemical complexity and diversity. Furthermore, nine target giant molecular clouds contain well-fit methanol emission, giving us a first look at the spatial chemical variability within the objects at relatively high (compared to past observations) resolutions of $\sim 5''$. This work lays the foundation for future high angular resolution studies of gas-phase chemistry with the full ALMA.

1 Introduction

Much of what is known about chemistry in star-forming regions comes from observations of nearby low-mass protostars, which have been found to host a wide range of molecules.[1–4] Such observations have shown that low-mass stars form in the coldest ($T \sim 10$ K) and densest ($n \sim 10^4$ cm^{-3}) cores. Orion KL, the closest massive star-forming region to the solar system at a distance of ~ 400 pc, is often considered the archetype of high-mass star-formation,[5] and several more distant, exceptionally bright molecular sources such as Sgr B2(N) ($d \sim 8$ kpc), W33A ($d \sim 4$ kpc), and W3(H$_2$O) ($d \sim 2$ kpc) have also been the subjects of repeated observations[6–8] but with concomitantly poorer linear spatial resolution.

The so-called molecular ring, which falls at radii of $\sim$4-8 kpc from the galactic center, has been mostly absent from astrochemical observations thus far despite containing the bulk of molecular matter in the Milky Way. Specifically, the surface density of giant H II regions along the galactic equator is highest between 4 and 8

kpc and peaks at $\sim$6 kpc.[9] Within this region of the galaxy, an estimated 85% of the gas is molecular.[10] This suggests that much of our understanding of interstellar chemistry neglects the regions of the Milky Way where most of the molecular chemistry proceeds. Thus, observations of such regions are imperative to answer questions about whether and how chemistry varies at different galactic radii. Moreover, including molecular-ring laboratories in the current astrochemical sample will push the field toward larger, and thus more statistically meaningful, sample sizes.

We present the pilot results of an unbiased molecular line survey carried out toward a sample of 11 giant molecular clouds (GMCs) in the molecular ring. These observations were carried out with the Atacama Compact Array (ACA), a dedicated subset of Atacama Large Millimeter/submillimeter Array (ALMA) antennas, to efficiently identify molecule-rich gas associated with potential young stellar objects (YSOs) and YSO candidates in anticipation of future high angular resolution studies of gas-phase chemistry with the full ALMA. In this pilot survey, six 1-GHz-wide spectral windows were used to get a first look at the chemical stockrooms in the targeted GMCs.

The sample is presented in Section 2, and the observations and data reduction are presented in Section 3. Section 4 presents an overview of the molecular line data and, where possible, derived methanol column densities and rotation temperatures. The chemical implications of these results are discussed in Section 5, where the results are also compared to previous literature. Finally, Sec-

California Institute of Technology, 1200 East California Boulevard, Pasadena CA 91125, USA.

* Corresponding author. Permanent E-mail: olivia.h.wilkins@outlook.com

† Electronic Supplementary Information (ESI) available as a PDF.

‡ Present address: NASA Postdoctoral Program Fellow, NASA Goddard Space Flight Center, 8800 Greenbelt Road, Greenbelt MD 20771, USA. E-mail: olivia.h.wilkins@nasa.gov

tion 6 summarizes the findings of this pilot survey.

2 Source Sample

The 11 sources observed in this study were selected from a sample of 437 GMCs with gas masses reported by Battisti and Heyer.[11] The GMCs were detected by the Bolocam Galactic Plane Survey (BGPS) of 1.1 mm dust continuum emission, and gas masses were derived from optically thin ^{13}CO $J = 1 - 0$ emission from the Five College Radio Astronomy Observatory (FCRAO) Galactic Plane Surveys.

The *Spitzer* c2d (Cores to Disks) survey confirmed a linear relationship between a cloud's mass surface density and the star formation rate therein, and further that star-forming regions are clustered about the densest cores.[12] As such, when building our sample, possible target GMCs were first screened for mass surface density

$$\Sigma_{GMC} = \frac{M_{GMC}}{\pi R_{GMC}^2} \quad (1)$$

where M_{GMC} is the mass and R_{GMC} is the effective radius of the cloud. A mass surface density of 200 $M_\odot$ pc^{-2} approximately corresponds to the 10^3 cm^{-3} density threshold for "dense" molecular clouds and was therefore used as the cut-off for selecting targets.

We then considered GMCs with radii $\leq 2.0''$ such that they could be observed with the ACA in a single session (i.e., with ≤ 150 pointings) and selected only those GMCs that fall within the molecular ring based on their celestial coordinates. This left us with a sample of 11 molecular-ring GMCs at kinematic distances of $d \sim 4$ kpc or $d \sim 11$ kpc . The properties of the observed targets are given in Table 1. For simplicity, we refer to these objects by their BGPS IDs throughout this paper; their official names are listed in column (2) of Table 1 for reference.

3 Observations

Observations of the 11 GMCs were carried out during Cycle 6 (Project Code: 2018.1.01259, P.I.: Wilkins) using the ACA, which is a subset of antennas from ALMA and uses up to twelve 7-meter antennas. For each source, there were two local oscillator (LO) settings in ALMA Band 6: the "lower" LO setting centered at $\sim$226 GHz and the "upper" centered at $\sim$251 GHz. These LO settings were chosen to target tracer and otherwise astrochemically-interesting compounds and also included a continuum window in each. Continuum windows had bandwidths of 2 GHz with 2048 channels. The passband was examined for excess line emission, and line-free channels across all spectral windows were used to measure the continuum flux. The ACA has an angular resolution of $5.''5-6.''2$ in the lower LO and $5.''2-5.''9$ in the upper LO setting. The mosaic fields of view were chosen based on GMC angular sizes reported by Battisti and Heyer.[11]

Calibration was completed using standard `CASA` (version 5.4.0-70) calibration pipeline scripts. The images presented here were primary-beam-corrected and created with continuum emission estimated from line-free channels and subtracted using the `tclean` algorithm with robust weighting and a Briggs parameter of 0.5 for deconvolution. The image noise-levels and synthesized beams are presented in Table 2. In general, the continuum noise level is ≤ 2.2 mJy beam^{-1}. A detailed description of the observations—
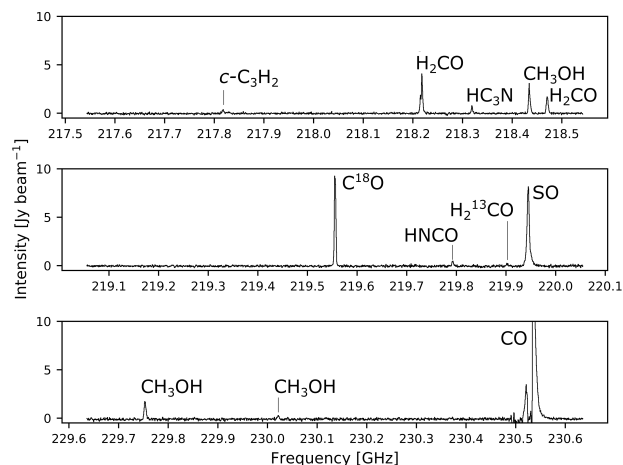

Fig. 1 ACA "lower" Band 6 spectra for BGPS 6120.

including calibrators, number of antennas, and dates—for each source can be found in the Supplementary Information.[†]

4 Results

4.1 Spectral Analysis

ACA spectra were inspected to compile a preliminary census of molecular compounds present in each source. Molecular transitions were identified using the Cologne Database for Molecular Spectroscopy (CDMS)[13–15] entries included in the Splatalogue[§] database for astronomical spectroscopy. Table 3 lists all identified transitions along with the GMC(s) where transitions were detected. Figure 1 shows the "lower" ALMA Band 6 spectra for BGPS 6120, which is one of the most chemically rich targets in our sample. A variety of molecular compounds are detected across the sample, including carbon monoxide (CO, $C^{18}O$), complex (having ≥ 6 atoms) organic compounds (CH$_3$OH, CH$_3$CCH), ionized species (H^{13}CO$^+$, HC^{18}O$^+$, HCS$^+$), nitrogen-bearing species (HC$_3$N), oxygen-bearing species (H$_2$CO, H$_2$^{13}CO), low gas density tracers (c-C$_3$H$_2$), and compounds formed in outflows (SO, SO$_2$, SiO).

As seen in Table 3, BGPS 6029 and BGPS 6120 are especially molecule-rich in this limited spectral line survey. BGPS 6318 is particularly molecule-poor, containing detectable CO and $C^{18}O$ emission only. For most compounds, only one line was present in our data. Multiple CH$_3$OH lines are detected in most sources. Several GMCs (BGPS 6029 and BGPS 6120) contain two lines of SO.

All sources except BGPS 6318 contain detectable CH$_3$OH and $C^{18}O$ emission concentrated around regions of 1.2 mm continuum emission. The targets (other than BGPS 6318) also all contain H$_2$CO, H^{13}CO$^+$, and SO. In this work, we focus on CH$_3$OH because multiple CH$_3$OH transitions are present in our data, allowing us to get a preliminary look at the gas temperature via spectral line fitting. Furthermore, CH$_3$OH is a hallmark of hot

Table 1 Properties of the 11 targeted GMCs

BGPS ID[a]	Name[a]	α^a_{J2000}	δ^a_{J2000}	v_{LSR} (km s^{-1})[a]	d_{kin} (kpc)[a,b]	R_{GMC} (pc)[a]	Σ_{GMC} ($M_\odot$ pc^{-2})[a]
3053	G023.368−00.290	18^{h}34^{m}53^{s}0	−08°37′43″	78.1	10.67 ± 2.50	5.17	352.50
3474	G025.227+00.289	18^{h}36^{m}15^{s}1	−06°42′50″	47.1	3.16 ± 0.73	1.61	233.32
4449	G030.536+00.021	18^{h}46^{m}53^{s}2	−02°07′22″	47.8	3.03 ± 0.14	1.53	258.36
5623	G030.952−00.389	18^{h}57^{m}05^{s}5	+02°06′44″	55.3	$10.49^{+1.32}_{-1.23}$	5.11	308.41
6029	G040.622−00.139	19^{h}06^{m}01^{s}3	+06°47′01″	32.8	11.01 ± 2.79	4.94	341.74
6082	G041.741+00.095	19^{h}07^{m}15^{s}1	+07°53′09″	13.7	11.91 ± 5.85	2.63	271.51
6112	G043.079−00.005	19^{h}10^{m}05^{s}7	+09°01′06″	14.2	11.65 ± 1.61	3.64	394.00
6120	G043.237−00.047	19^{h}10^{m}33^{s}0	+09°08′12″	7.5	12.04 ± 2.72	5.28	682.78
6299	G049.070−00.350	19^{h}22^{m}46^{s}3	+14°09′25″	66.0	5.57 ± 1.25	1.66	323.44
6310	G049.170−00.208	19^{h}22^{m}26^{s}3	+14°19′26″	63.1	5.56 ± 0.86	2.67	589.39
6318	G049.255−00.412	19^{h}23^{m}21^{s}0	+14°17′54″	66.3	5.55 ± 1.06	1.48	508.62

[a] Values taken from Battisti and Heyer.[11] [b] The uncertainties for d_{kin} were not reported by Battisti and Heyer but were calculated for use in this work following the procedure given in the Supplementary Information.[†] [c] Calculated using Equation 1.

Table 2 ACA image properties

BGPS ID	$\sigma_{RMS,cont}$ (mJy beam^{-1})	θ_{syn}	Field of View
3053	1.7	5″9×3″8	210″×210″
3474	1.6	6″3×4″0	216″×216″
4449	1.6	6″7×3″9	210″×210″
5623	2.2	9″4×4″1	210″×210″
6029	1.9	7″1×4″2	180″×180″
6082	1.4	6″4×3″8	145″×145″
6112	1.2	7″5×4″7	163″×163″
6120	1.4	7″2×4″7	186″×186″
6299	1.8	7″4×4″4	165″×165″
6310	1.2	6″3×4″7	254″×254″
6318	1.5	8″2×2″5	145″×145″

molecular cores,[2] signalling places where there may be new organic chemistry laboratories in the molecular ring.

Figure 2 shows the regions where we see both C^{18}O (a tracer of dense regions, such as cores)[16] and CH$_3$OH (commonly used as a tracer of other complex organics).[2,17] Each panel is labeled by its BGPS ID and an ACA# ID. For GMCs with multiple millimeter-emitting regions shown, the # was assigned by decreasing peak continuum flux. These regions are listed in Table 4

4.2 CH$_3$OH Rotation Temperatures and Column Densities

Figures 3-11 show the derived rotation temperature T_{rot} and column density N_{tot} maps for CH$_3$OH toward nine of the 11 target GMCs. Each map shows the entire ACA field of view (listed in Table 2) for each target. As mentioned in Section 4.1, BGPS 6318 did not contain CH$_3$OH emission. BGPS 6082 is also not represented in the figures because the lines in those spectra were too noisy to be fit successfully. Percent propagated uncertainty maps are presented in the Supplementary Information[†] and show that most fitted objects have fit uncertainties of ≤10% near the co-spatial continuum emission peaks.

The rotation temperature and column density maps were derived using a pixel-by-pixel fit of the spectra extracted within a single synthesized beam centered on each pixel. This follows the same procedure as Wilkins et al.[18] and is briefly described here. To avoid erroneous fits, only lines with peak amplitudes of ≥3σ_{RMS} were considered. Rotation temperature T_{rot} [K] and column density N_{tot} [cm^{-2}], along with line width and velocity shift, were determined simultaneously by least-squares fitting with LMFIT[19] (version 0.9.15) to model the spectra assuming op-

tically thin lines at local thermodynamic equilibrium (LTE); commentary on the robustness of the LTE assumption is given in Section 4.3. The spectra were modeled using Equation 2 adapted from Remijan et al.[20]

$$N_{tot} = 2.04 \times 10^{20} C_\tau \frac{1}{\Omega_S(\Omega_S + \Omega_B)} \frac{\int I_\nu d\nu}{\theta_a \theta_b} \frac{Q(T_{rot})e^{E_u/T_{rot}}}{\nu^3 S_{ij}\mu^2} \text{ cm}^{-2} \quad (2)$$

where the $\int I_\nu d\nu$ is the integrated intensity of the line [Jy beam^{-1} km s^{-1}], the optical depth correction factor $C_\tau = \tau/(1-e^{-\tau})$ is assumed to be unity (since we assume the optical depth τ is small), Ω_S and Ω_B are the solid angles of the source and beam respectively, θ_a and θ_b are the synthesized beam sizes [″], Q is the partition function, E_u is the upper-state energy level [K], ν is the rest frequency of the transition [GHz], and $S_{ij}\mu^2$ is the product of the transition line strength and the square of the electric dipole moment [Debye^2]. The lines fit in this analysis are given in Table 5.

We assume that the source fills the beam at all positions and that $\Omega \approx \pi\theta^2$ since θ is small ($\sim$5″), with the caveat that, because the objects targeted are overall not well characterized in the existing literature, this may not be a robust assumption; if there are objects in the sample where the source does not fill the beam, emission from those objects may be diluted in our beam and our column density calculations may be lower limits. However, since the work described here is part of a pilot survey, the goal is to identify regions for follow-up high-resolution observations.

As seen in Figures 3-11, the derived rotation temperature is less than 20 K for most objects. Under the assumptions of LTE, we can approximate the kinetic temperature of the objects by the rotation temperature. At the angular resolution of the ACA, we resolve the structure within the target sample GMCs on linear scales of $\sim$10^4-10^5 au. These large scales correspond to the spatial scales of dense clumps but are too large to resolve individual protostars; as such, these low temperatures are expected because warmer protostellar gas will be diluted by colder gas in the envelope.

Two sources—BGPS 6029 (Figure 7) and BGPS 6120 (Figure 9)—have higher temperatures of up to 40 K and 35 K, respectively. These are still sub-hot core temperatures, but are warmer than the $\sim$10 K of the interstellar gas in which the seeds of infant stars are planted. This may indicate that the objects in these sources are more evolved and contain cores that are undergoing warm-up. As seen in Table 3, BGPS 6029 and BGPS 6120 are

Table 3 Molecules with at least one transition detected toward the target GMCs

Molecule	Transition	Frequency (GHz)	BGPS ID										
			3053	3474	4449	5623	6029	6082	6112	6120	6299	6310	6318
CO	$2-1, v=0$	230.538	X	X	X	X	X	X	X	X	X	X	X
$C^{18}O$	$2-1, v=0$	219.560	X	X	X	X	X	X	X	X	X	X	X
SO	6_5-5_4	219.949	X	X	X	X	X	X	X	X	X	X	...
SiO	$6-5$	260.518	...	...	...	X	X	...	X	X	...	...	...
SO_2	$5_{(2,4)}-4_{(1,3)}$	241.616	...	...	...	...	X	...	...	X	...	...	...
	$4_{(3,1)}-4_{(2,2)}$	255.553	...	...	...	...	X	...	...	X	...	...	...
HDO	$2_{(1,1)}-2_{(1,2)}$	241.562	...	...	...	...	X	...	...	...	...	...	...
	$5_{(3,3)}-5_{(2,4)}$	256.247	...	...	...	...	X	...	...	X	...	...	...
HCS^+	$6-5$	256.027	...	...	...	...	X	...	...	X	...	...	...
$H^{13}CO^+$	$3-2$	260.255	X	X	X	X	X	X	X	X	X	X	...
$HC^{18}O^+$	$3-2$	255.479	...	...	...	...	X	...	...	X	...	...	...
H_2CO	$3_{(0,3)}-2_{(0,2)}$	218.222	X	X	X	X	X	X	X	X	X	X	...
	$3_{(2,2)}-2_{(2,1)}$	218.476	X	X	X	X	X	X	X	X	X	X	...
$H_2{}^{13}CO$	$3_{(1,2)}-2_{(1,1)}$	219.909	...	X	...	...	X	...	...	X	...	...	...
HNCO	$10_{(0,10)}-9_{(0,9)}$	219.798	...	X	...	...	X	...	...	X	...	...	...
HC_3N	$24-23$	218.325	...	X	...	...	X	...	...	...	...	...	...
c-C_3H_2	$6_{(1,5)}-5_{(0,5)}$	217.822	X	X	X	X	X	...	...	X	...	...	...
	$5_{(1,4)}-4_{(2,3)}$	217.940	...	X	X	X	X	...	...	...	...	...	...
CH_3OH	$4_{(-2,3)}-3_{(-1,2)}$ E	218.440	X	X	X	X	X	X	X	X	X	X	...
	$8_{(1,8)}-7_{(-0,7)}$ E	229.759	...	X	X	X	X	...	X	X	X	...	...
	$3_{(2,1)}-4_{(1,4)}$ E	230.027	...	...	...	X	X	...	...	X	...	...	...
	$5_{(-0,5)}-4_{(-0,4)}$ E	241.700	X	X	X	X	X	...	X	X	X	X	...
	$5_{(1,5)}-4_{(1,4)}$ E	241.767	X	X	X	X	X	X	X	X	X	X	...
	$5_{(0,5)}-4_{(0,4)}$ A	241.791	X	X	X	X	X	X	X	X	X	X	...
	$5_{(4,2)}-5_{(4,1)}$ A	241.807	...	...	...	...	X	...	...	...	...	...	...
	$5_{(4,2)}-5_{(4,1)}$ E	241.813	...	...	...	...	X	...	...	...	...	...	...
	$5_{(3,2)}-4_{(3,1)}$ A	241.833	...	...	...	...	X	...	...	X	...	...	...
	$5_{(2,4)}-4_{(2,3)}$ A	241.842	...	...	...	...	X	...	...	X	...	...	...
	$5_{(3,2)}-4_{(3,1)}$ E	241.852	...	...	...	...	X	...	...	...	...	...	...
	$5_{(-1,4)}-4_{(-1,3)}$ E	241.879	X	X	...	X	X	...	X	X	...	...	...
	$5_{(2,3)}-4_{(2,2)}$ A	241.888	...	...	...	...	X	...	...	X	...	...	...
	$5_{(-2,4)}-4_{(-2,3)}$ E	241.905	X	X	X	X	X	X	X	X	X	X	...
CH_3CCH	15_3-14_3	256.293	...	...	...	...	X	...	...	X	...	...	...
	15_2-14_2	256.317	...	...	...	...	X	...	...	X	...	...	...
	15_1-14_1	256.332	...	...	X	...	X	...	...	X	...	...	...
	15_0-14_0	256.337	...	...	X	...	X	...	...	X	...	...	...

Table 4 ALMA Band 6 (245 GHz, 1.2 mm) continuum emission regions with both $C^{18}O$ and CH_3OH emission

Source	α_{J2000}	δ_{J2000}	S_{peak} (mJy beam^{-1})	τ	C_τ
BGPS 3053 ACA1	$18^h34^m54^s10$	$-08°38'24''1$	67.3	0.06	1.03
BGPS 3053 ACA2	$18^h34^m49^s66$	$-08°38'28''9$	18.1	0.04	1.02
BGPS 3474 ACA1	$18^h36^m16^s76$	$-06°43'18''5$	206.9	0.34	1.18
BGPS 4449 ACA1^a (N)	$18^h46^m59^s39$	$-02°07'25''1$	273.6	0.04	1.02
(S)				0.06	1.03
BGPS 4449 ACA2	$18^h46^m55^s18$	$-02°08'17''7$	44.2	0.04	1.02
BGPS 5623 ACA1	$18^h57^m05^s29$	$+02°06'30''1$	121.2	0.13	1.07
BGPS 6029 ACA1	$19^h06^m01^s54$	$+06°46'35''2$	386.6	0.04	1.02
BGPS 6112 ACA1	$19^h10^m04^s40$	$+09°01'12''3$	68.3	0.08	1.04
BGPS 6112 ACA2	$19^h10^m07^s72$	$+09°01'16''5$	32.0	0.05	1.02
BGPS 6112 ACA3	$19^h10^m05^s92$	$+09°01'16''0$	19.9	0.02	1.01
BGPS 6120 ACA1	$19^h10^m33^s69$	$+09°08'23''3$	509.1	0.03	1.02
BGPS 6299 ACA1	$19^h22^m42^s43$	$+14°09'53''1$	43.3	0.18	1.10
BGPS 6310 ACA1	$19^h22^m26^s99$	$+14°18'47''3$	60.5	0.16	1.08
BGPS 6310 ACA2	$19^h22^m26^s87$	$+14°17'40''2$	26.7	0.08	1.04

^{a} BGPS 4449 ACA1 contains two distinct CH_3OH peaks, labeled N (north) and S (south). The optical depth τ values are listed for each CH_3OH peak. The coordinates and peak flux given are for the entire ACA1 continuum emission region.

Table 5 CH_3OH lines fit to derive column density and rotation temperature

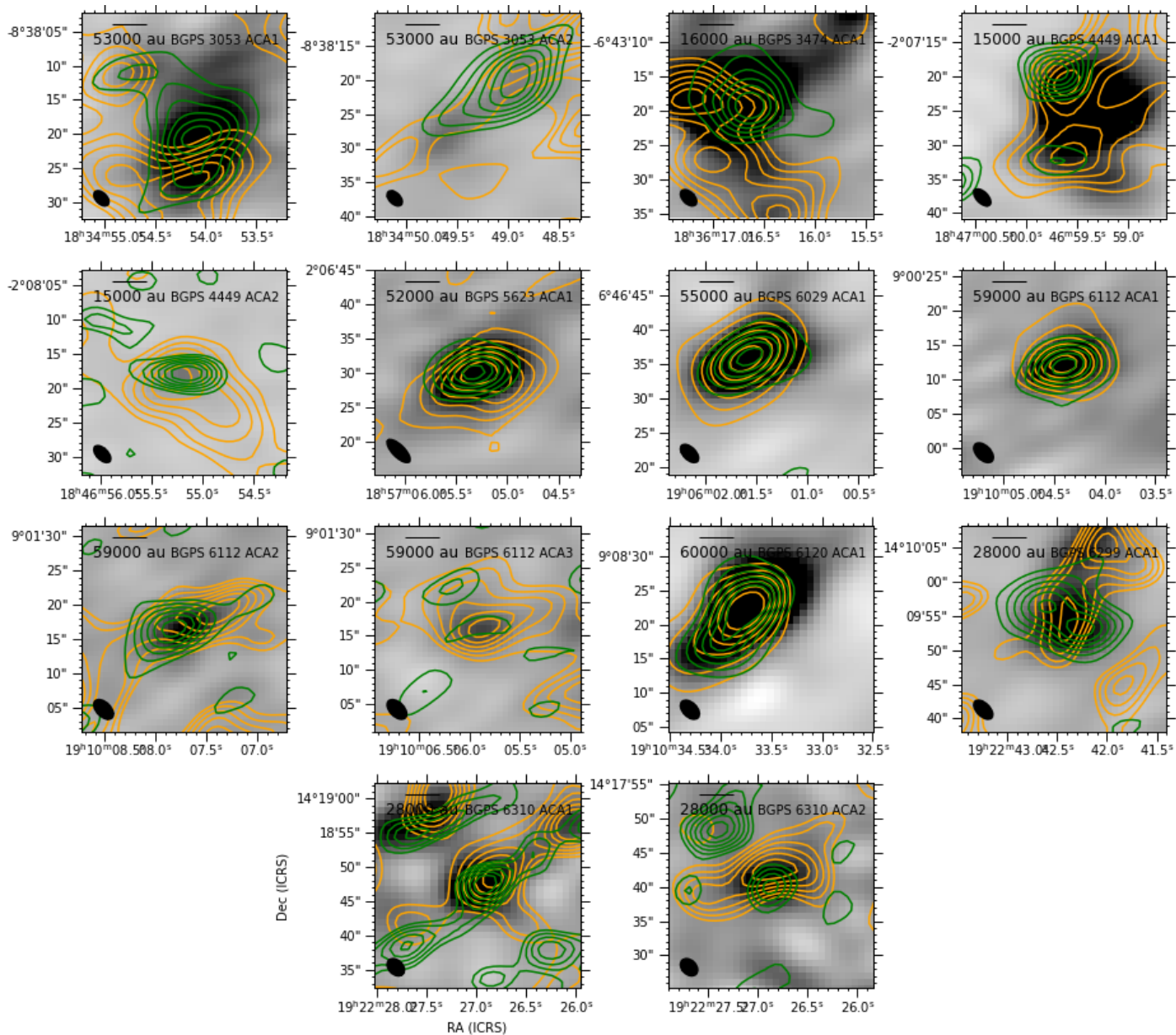| Transition	ν (GHz)	E_u (K)	g_u	A_{ul} (s^{-1})	$S_{ij}\mu^2$ (Debye^2)
$5_{(-0,5)}-4_{(-0,4)}$, E	241.7002	47.93	44	6.03×10^{-5}	16.16
$5_{(1,5)}-4_{(1,4)}$, E	241.7672	40.39	44	5.81×10^{-5}	15.53
$5_{(0,5)}-4_{(0,4)}$, A	241.7914	34.82	44	6.04×10^{-5}	16.17
$5_{(-1,4)}-4_{(-1,3)}$, E	241.8790	55.87	44	5.96×10^{-5}	15.92
$5_{(-2,4)}-4_{(-2,3)}$, E	241.9046	57.07	44	5.03×10^{-5}	13.43

Fig. 2 Contours showing the distribution of $C^{18}O$ (orange) and CH_3OH (green) emission, represented by the integrated intensities of the 219.560 and 218.440 GHz lines, respectively, in mm sources. The greyscale images show the Band 6 ($\sim$240 GHz) continuum. The black ellipse in the bottom left of each panel shows the synthesized beam size.
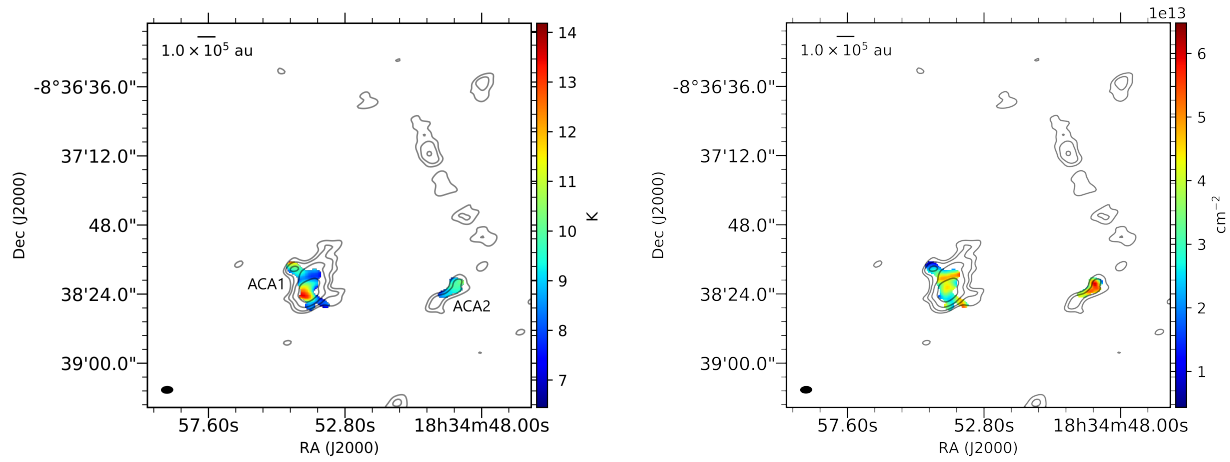
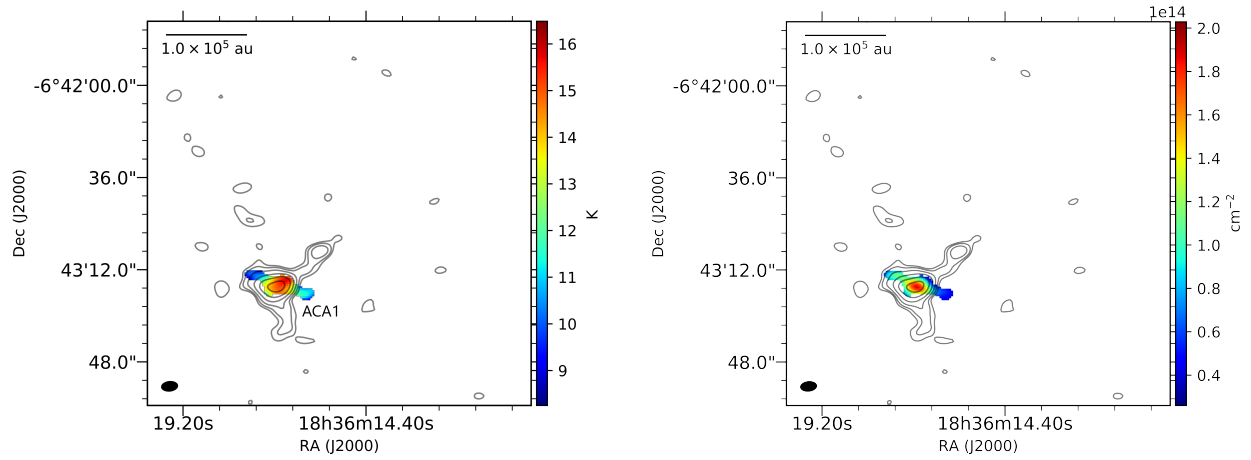Fig. 3 Derived rotation temperature (left) and column density (right) for CH$_3$OH in BGPS 3053.

Fig. 4 Derived rotation temperature (left) and column density (right) for CH$_3$OH in BGPS 3474.
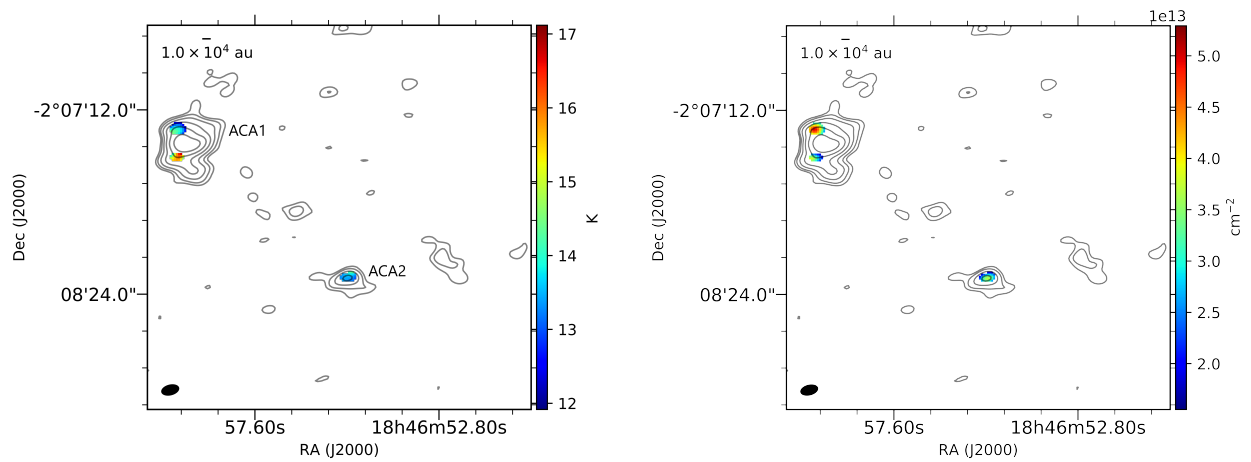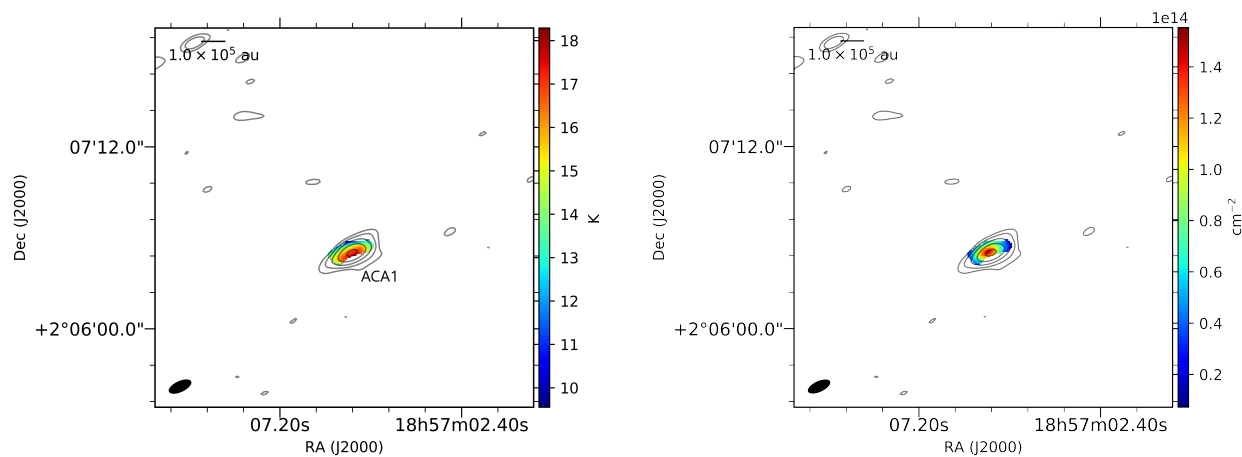

Fig. 5 Derived rotation temperature (left) and column density (right) for CH$_3$OH in BGPS 4449.

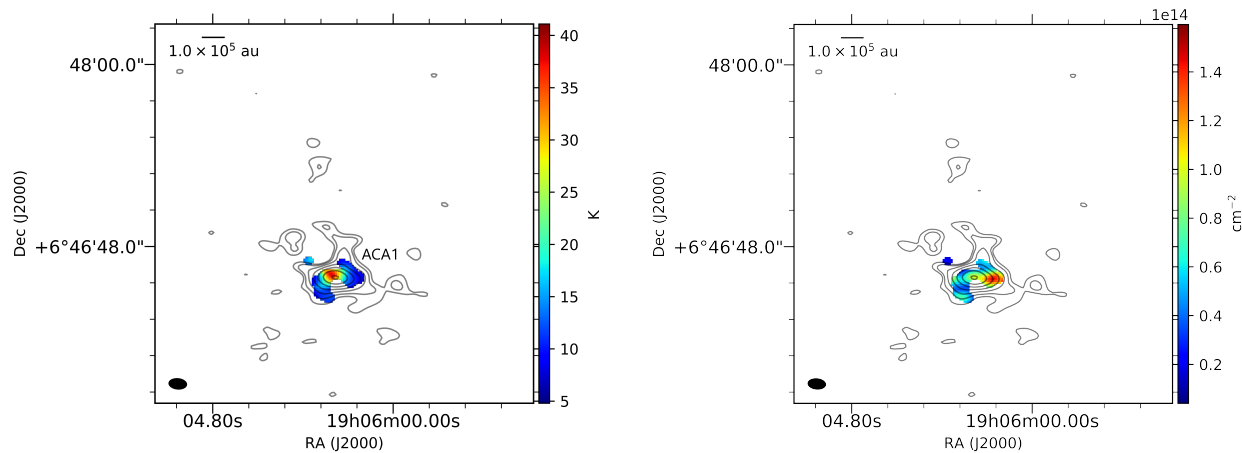Fig. 6 Derived rotation temperature (left) and column density (right) for CH$_3$OH in BGPS 5623.

Fig. 7 Derived rotation temperature (left) and column density (right) for CH$_3$OH in BGPS 6029.

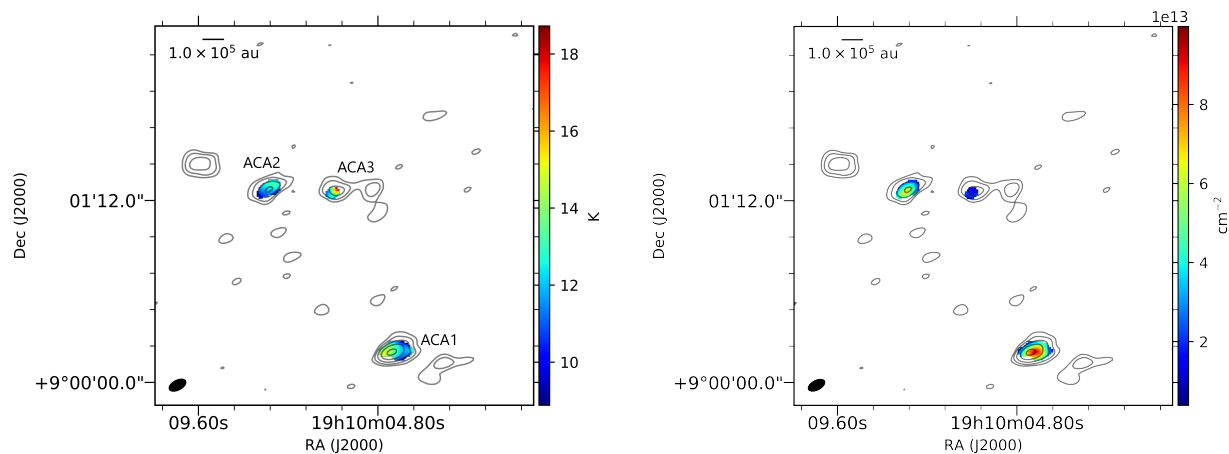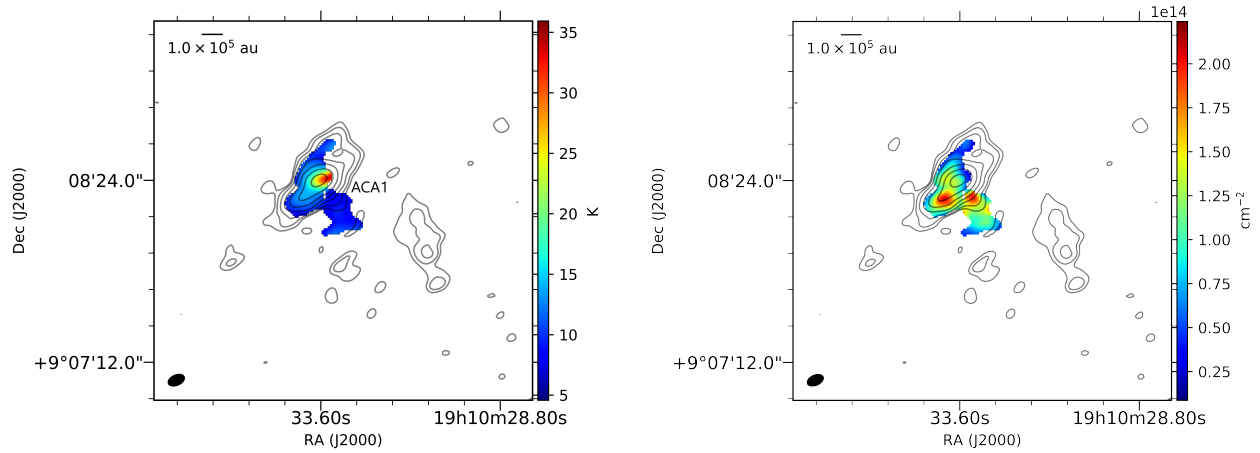Fig. 8 Derived rotation temperature (left) and column density (right) for CH$_3$OH in BGPS 6112.

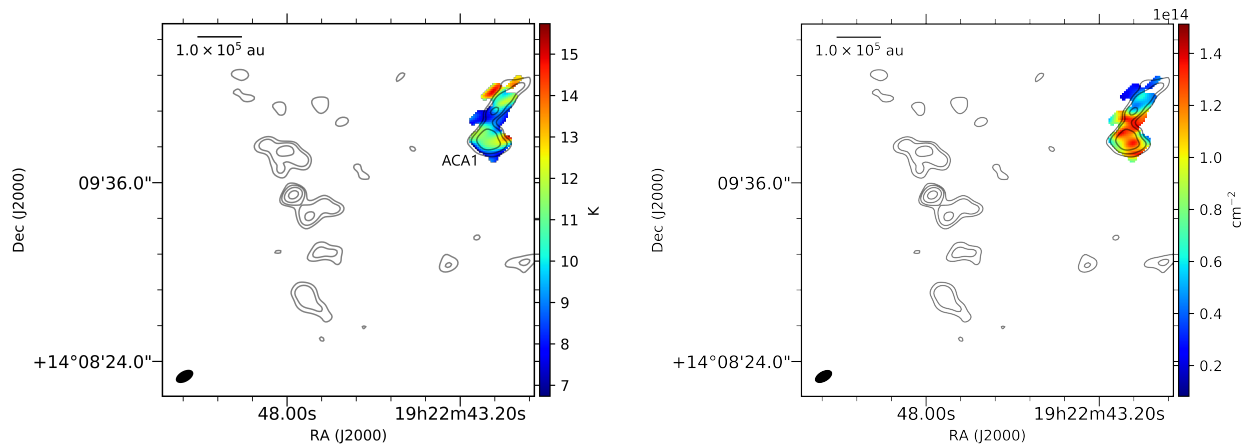Fig. 9 Derived rotation temperature (left) and column density (right) for CH$_3$OH in BGPS 6120.

Fig. 10 Derived rotation temperature (left) and column density (right) for CH$_3$OH in BGPS 6299.

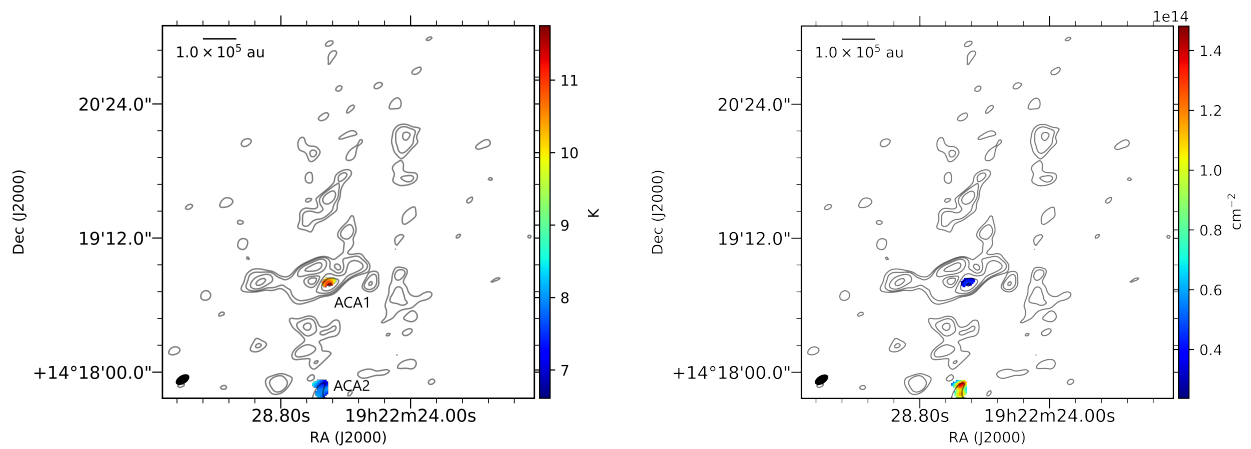Fig. 11 Derived rotation temperature (left) and column density (right) for CH$_3$OH in BGPS 6310.

also the most chemically rich in our sample, which is a further sign that these regions may be more evolved than other regions identified in the sample.

CH$_3$OH column densities N_{tot} were derived to be on the order of 10^{13}-10^{14} cm^{-2}, which is similar to abundances calculated for prestellar cores.[21] For the most part, the sources exhibit a single peak in column density that is co-spatial with the millimeter continuum emission peak. This is the case for BGPS 3474 ACA1 (Figure 4), BGPS 4449 ACA2 (Figure 5), BGPS 5623 ACA1 (Figure 6), BGPS 6112 ACA1, BGPS 6112 ACA2, BGPS 6112 ACA3 (Figure 8), BGPS 6310 ACA1, and BGPS 6310 ACA2 (Figure 11). The remaining sources—BGPS 4449 ACA1 (Figure 5), BGPS 6029 ACA1 (Figure 7), BGPS6120 ACA1 (Figure 9), and BGPS 6299 ACA1 (Figure 10)—have more peculiar N_{tot}(CH$_3$OH) profiles.

BGPS 4449 ACA1 (Figure 5) shows two fittable CH$_3$OH emission regions, indicating that this object may contain not one but two molecular cores. Ellsworth-Bowers et al.[22] reported a dense core in this region, and Saral et al.[23] identified this location as the site of a YSO and YSO candidates. In our analysis, the two candidate cores have different temperature and column density profiles. The northern source is slightly colder (13-14 K) but with a higher peak CH$_3$OH column density of $\sim 5.0 \times 10^{13}$ cm^{-2}. The southern source has temperature approaching 17 K but column densities about a factor of two lower than the northern source.

The peak column density ($\sim 1.4 \times 10^{14}$ cm^{-2}) in BGPS 6029 ACA1 is off-center to the west[¶] of the continuum emission peak. This is particularly curious because the maximum temperature (~ 40 K) in that region is nonetheless co-spatial with the continuum peak. The peaks in the measured parameters have uncertainties of $\leq 10\%$ (see the Supplementary Information[†]), so this profile is not likely the result of poor spectral line fits. Instead, we may be seeing the overall temperature of a cluster of multiple objects early in stellar evolution. For instance, BGPS 6029 ACA1 reportedly corresponds to dense cores[24,25] and a YSO.[26,27] Lu et al.[25] report three distinct cores with radii of ~ 0.03 pc (~ 6000 au) from VLA ammonia (NH$_3$) observations. Fontani et al.[28] observed BGPS 6029 ACA1 as part of an astrochemical study to understand the nature of deuterium chemistry in high-mass star-forming regions. However, Fontani et al. could not find deuterated methanol, which they used as a tracer of high-mass protostellar objects in which molecules formed through grain-surface chemistry are sputtered from the icy grain mantles, and concluded that the region is too evolved for grain-surface chemistry to be observed.

Like BGPS 4449 ACA1, the millimeter continuum region BGPS 6120 ACA1 (Figure 9) contains multiple methanol column density peaks. There are two column density peaks of $\sim 2.0 \times 10^{14}$ cm^{-2} to the southeast and southwest of the continuum emission peak. There is another local peak with $N_{tot} \sim 1.5 \times 10^{14}$ cm^{-2} just to the east of the continuum peak. This agrees with past large surveys that reveal structures related to the early stages of star formation. For example, Morales et al.[30] characterized a partially embedded cluster about 66″ across in BGPS 6120. There are multiple YSOs

and YSO candidates reported there as well.[23,31] Saral et al.[23] specifically report five YSO candidates. Our map of CH$_3$OH column density supports 2-3 of these being molecular cores.

BGPS 6299 ACA1 (Figure 10) is perhaps the most abnormal fitted region in our data. It appears to be a complex comprising multiple millimeter continuum peaks. There are two regions with rotation temperatures of ~ 12-15 K separated by a band of 7-8 K. Surprisingly, the cold band coincides with a region where N_{tot}(CH$_3$OH) $\sim 1.4 \times 10^{14}$ cm^{-2} that stretches south. North of the cold band, $N_{tot} \sim 6 \times 10^{13}$ cm^{-2}. The northern aspect of BGPS 6299 ACA1 has higher uncertainties of $\sim 20\%$ whereas the cold band and the region south of it are fit well with uncertainties of $\leq 5\%$. The higher uncertainty to the north may be because the emission falls at the edge of the ACA's field of view and is thus noisier. In the south, the high-density region is broken up into several smaller regions, which may be indicative of a young stellar cluster. This is consistent with the existing literature, which reports five YSOs or YSO candidates in the vicinity of BGPS 6299 ACA1.[32,33] This region has also been reported to contain a dense core with a 1.00 probability of star formation as well as a H$_2$O maser.[26,32]

In summary, across the nine GMCs containing fittable CH$_3$OH emission, there are ≥ 15 apparent molecular cores with CH$_3$OH column densities of 10^{13}-10^{14} cm^{-2}. In general, derived rotation temperatures are ≤ 20 K, but a couple regions have higher temperatures of ~ 40 K.

4.3 Optical Depth and LTE Assumptions

The analysis in the previous section assumes that all observed CH$_3$OH emission is optically thin. However, CH$_3$OH is notoriously optically thick toward protostars.[8,34] Given the colder temperatures detected here, optically thin CH$_3$OH may be a more valid assumption, as is the case toward low-mass YSOs and cold prestellar cores.[4,21]

We tested this assumption by comparing the fitted parameters (N_{tot}, T_{rot}) to the CH$_3$OH spectrum for a pixel of near the center of each emission region. The optical depth τ of a line can be calculated as

$$\tau = \frac{g_u}{\Delta V} \frac{N_{tot}}{Q(T_{rot})} \frac{A_{ul} c^3}{8\pi\nu^3} e^{-E_u/T_{rot}} \left(e^{h\nu/kT_{rot}} - 1 \right) \qquad (3)$$

where g_u is the degeneracy of the upper state, ΔV is the fitted line width, A_{ul} is the Einstein A coefficient, h is the Planck constant, and k is the Boltzmann constant. Other terms are the same as in Equation 2. Optical depth was calculated for each of the five lines listed in Table 5. From this, the optical depth correction factor $C_\tau = \tau/(1 - e^{-\tau})$ was calculated. Both τ and C_τ were averaged for each target and are summarized in Table 4.

Most sources in our sample have $\tau \ll 1$ or $C_\tau \sim 1$, confirming that the emission is indeed optically thin. A few sources, notably BGPS 3474 ACA1 ($C_\tau = 1.18$) and BGPS 6299 ACA1 ($C_\tau = 1.10$), have higher optical depth factors, suggesting CH$_3$OH may be optically thick toward the millimeter emission peaks, which would in turn result in the column densities being lower limits. Nonetheless, the assumption that the analyzed lines are optically thin is

---

[¶] In astronomical maps, north is up, south is down, west is right, and east is left.

sufficient to achieve the present work's goal of gaining a preliminary look at the chemistry in previously unexplored interstellar laboratories.

Another consideration is the degree to which excitation, specifically rotation, temperatures T_{rot} reflect the kinetic temperatures T_{kin} in the targeted regions. This assumption typically holds in dense star-forming regions where $n_H \sim 10^5$-10^6 cm^{-3}. However, because the regions in our sample are not yet well characterized, making such an assumption is difficult. As discussed in Section 2, the target GMCs were screened to have mass surface densities ≥ 200 $M_\odot$ pc^{-2}, which approximately corresponds to $n_H \geq 10^3$ cm^{-3}. The mass surface density threshold is averaged over the entire field of view observed with the ACA, meaning that the continuum emission regions in which we fit the CH$_3$OH spectra are even denser. Many of these objects are associated with known YSOs or YSO candidates in other, large surveys,[27,32,33] suggesting a high density assumption is reasonable. Again, we stress that the purpose of this work is to survey the target GMCs for follow-up high-angular resolution studies, so the assumptions made here are sufficient.

4.4 SiO Distribution

Silicon monoxide (SiO) is a reliable tracer of shock chemistry, particularly that associated with protostellar outflows.[35] SiO is produced in the gas phase from Si-bearing material sputtered off dust grains, from either the grain mantles or cores.[36] The rate of SiO production has been further shown to be influenced by the sputtering of other simple molecules, such as CO.[37]

As indicated in Table 3, SiO was detected in only a few sources in our sample: BGPS 5623, BGPS 6029, BGPS 6112, and BGPS 6120. The distribution of SiO in these GMCs is illustrated in Figure 12. Of these, BGPS 6029 and BGPS 6120 were identified as being the most chemically rich, as well as the warmest, sources in the sample, which may indicate that these sources are more evolved than the others in the sample. Furthermore, BGPS 6029 ACA1 and BGPS 6120 ACA1 have been previously identified as active star-forming regions.[23,26,27] Thus, the presence of SiO emission, which has significantly enhanced abundances in protostellar outflows,[37–39] is to be expected.

Compared to other sources in our sample, BGPS 5623 ACA1 and BGPS 6112 ACA1 are not exceptional in terms of molecular diversity (Table 3) and temperature profile (Figures 6 and 8, respectively). However, the presence of detectable SiO emission overlapping with the organic material traced by CH$_3$OH, as seen in the left column of Figure 12, supports previous reports of YSOs in these regions.[31,32,40,41] This may also indicate that the YSOs therein are more evolved than other sources in the sample. However, the absence of a SiO detection toward other sources does not definitively preclude its presence.

4.5 *c*-C$_3$H$_2$ Distribution

Cyclopropenylidene (*c*-C$_3$H$_2$) has been suggested as a tracer of cold material in molecular clouds.[42] Observations of this molecule in L1544 showed that not only does it trace colder gas than CH$_3$OH, it originates in the outer, less dense layers of prestel-

lar cores.[43]

We detected *c*-C$_3$H$_2$ in BGPS 3053, BGPS 3474, BGPS 4449, BGPS 5623, and BGPS 6029. Figure 13 shows the distribution of *c*-C$_3$H$_2$ (cyan contours) in these GMCs, with the CH$_3$OH distribution (green contours) shown for comparison. In three sources— BGPS 3474 ACA1, BGPS 5623 ACA1, and BGPS 6029 ACA1— the *c*-C$_3$H$_2$ emission peaks coincide with the CH$_3$OH peaks. In BGPS 3474 ACA1, the distribution of *c*-C$_3$H$_2$ is slightly less extended than CH$_3$OH, particularly toward the northern and southern edges of the 1.2 mm continuum emission region. In BGPS 5623 ACA1, the *c*-C$_3$H$_2$ emission peak is slightly west of the CH$_3$OH peak, but the distributions of these two molecules otherwise have similar spatial profiles. In BGPS 6029 ACA1, however, the *c*-C$_3$H$_2$ emission is more extended than that of CH$_3$OH, stretching toward the north and west. In these directions, there are also *c*-C$_3$H$_2$ emission peaks cospatial with continuum emission; these regions could could perhaps correspond to prestellar cores in which CH$_3$OH has not yet formed or has not yet been liberated from the dust grains.

The *c*-C$_3$H$_2$ and CH$_3$OH profiles are much different in BGPS 3053 ACA1 and BGPS 4449 ACA1. There are at least two CH$_3$OH emission peaks in BGPS 3053 ACA1, including one centered on the strongest 1.2 mm continuum emission region. The second CH$_3$OH peak lies to the northeast and coincides with a continuum emission region that is somewhat separated from the larger complex. In this source, *c*-C$_3$H$_2$ has at least four peak emission regions. Only one is cospatial with a CH$_3$OH emission peak, specifically that to the northeast. The remaining three are distributed across the main continuum region, with the strongest peak lying to the south of the CH$_3$OH peak.

Similarly, the *c*-C$_3$H$_2$ and CH$_3$OH distributions do not have overlapping profiles in BGPS 4449 ACA1. In this source, the CH$_3$OH emission has distinct north and south peaks, whereas the *c*-C$_3$H$_2$ emission is more extended and spans the entire BGPS 4449 ACA1 1.2 mm continuum region. This molecular emission may thus trace the colder gas enveloping the two molecular cores traced by CH$_3$OH.

5 Discussion

The maps presented in Section 4 reveal a number of previously unexplored astrochemical laboratories in the molecular ring. Except for BGPS 6029 (in which NH$_3$ was previously observed[25]), the objects targeted in this pilot survey have not, as far as we know, been previously observed in terms of molecular emission. From this first look at the spectral line emission in these molecular-ring GMCs, we see a rich display of chemistry, including so-called complex organics, ionized species, nitrogen-bearing species, and tracers of protostellar outflows.

5.1 Possible Snapshots of Protostellar Evolution

From the chemical inventories and integrated intensity and fitted parameter maps, we see that there may be objects at different stages of stellar evolution across different GMCs in the sample (i.e., the warmer and more chemically-rich BGPS 6029 and BGPS 6120 in contrast with the colder and relatively molecule-
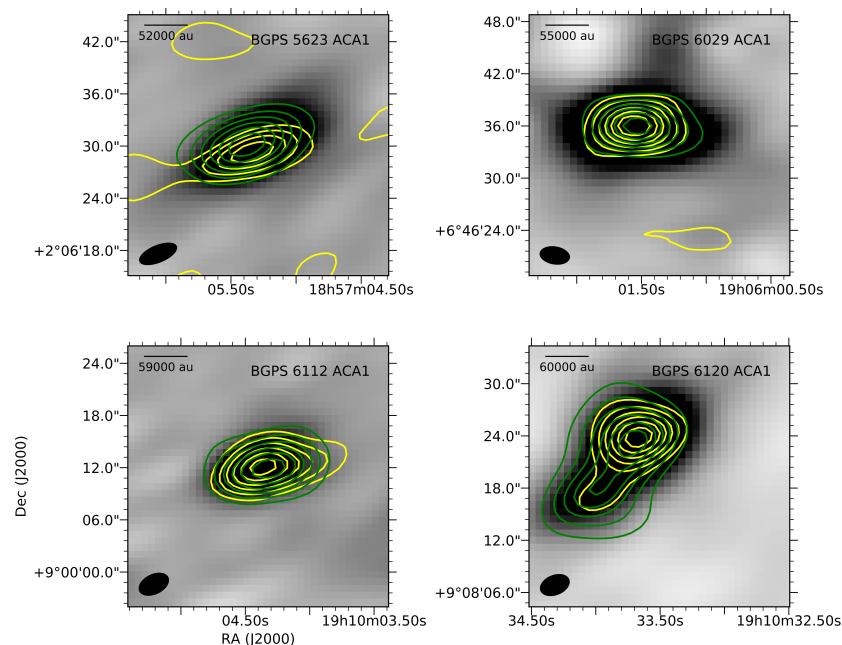
Fig. 12 Distribution of SiO showed by yellow contours compared to CH_3OH emission (green contours), represented by the integrated intensities of the 260.518 and 218.440 GHz lines, respectively. The underlying greyscale images show the Band 6 (~240 GHz) continuum. The black ellipse in the bottom left of each panel shows the synthesized beam size.

poor BGPS 6310). For GMCs in which multiple YSOs and YSO candidates have been identified, there is evidence of a range of YSO stages within the individual clouds. Specifically, BGPS 6120 ACA1 contains multiple CH_3OH column density peaks that span a range of rotation temperatures from <10 K to ~30 K (Figure 9). Furthermore, the SiO emission in this region (Figure 12) is less extended than that of CH_3OH and is concentrated near where the rotation temperature in ACA1 is the warmest, which may indicate more evolved material to the northwest of the ACA1 continuum region and less evolved material to the southeast.

The detection of SiO in BGPS 5623 ACA1 and BGPS 6112 ACA1 is also interesting. The other two targets in our sample with detectable SiO emission are also the most molecule-rich, but BGPS 5623 and BGPS 6112 each have about half the number of of detected molecular species as BGPS 6029 and BGPS 6120 in this survey. This, along with the derived rotation temperatures for these sources, is characteristic of many of the other observed sample targets. It is possible, then, that the combination of SiO emission and cold temperatures in BGPS 5623 ACA1 and BGPS 6112 ACA1 means these objects are in an evolutionary state between those of BGPS 6029 ACA1 and BGPS 6120 ACA1 and of the CH_3OH-containing objects in which SiO was not detected. If this is the case, the sample provides several snapshots along the evolutionary sequence of YSOs in molecular-ring star-forming regions.

Furthermore, while BGPS 6112 ACA1 has detectable SiO emission, its ACA2 and ACA3 counterparts do not. This may be because BGPS 6112 ACA2 and ACA3 are, respectively, not as evolved as and more evolved than BGPS 6112 ACA1. ACA2 is slightly colder than the other two BGPS 6112 molecular emission regions (Figure 9), and its classification as a Class I YSO candidate[23] may mean that it is too early in its evolution to be

emitting detectable molecular outflows traced by SiO emission. Conversely, ACA3 is slightly warmer than ACA1 and has been classified as a Class II YSO;[23] as such, ACA3 may be nearing the end of its protostellar evolution.

Other evolutionary clues may come from c-C_3H_2 emission. The extended c-C_3H_2 emission and absence of detectable SiO emission in the northeast of BGPS 3053 ACA1 and between BGPS 4449 ACA1(N) and ACA1(S) may indicate early-stage star formation, perhaps at the prestellar stage, is present in these regions. Similarly, while BGPS 6029 ACA1 contains SiO emission, it is confined to the strongest 1.2 mm continuum emission region; the c-C_3H_2 emission is much more extended, with two cold regions to the north and west extending from the warmer CH_3OH region, suggesting this source could be a site to study how chemistry varies with temperature within a single object.

5.2 Comparison to Other Sources

Curiously, even the warmest regions (based on fitted CH_3OH emission) in our sample are at most ~40 K, well below typical rotation temperatures of ≥100 K for CH_3OH in hot cores such as AFGL 2591 ($d \sim 3.3$ kpc)[44], NGC 7538 IRS1 ($d \sim 2.6$ kpc)[45], and the Orion KL Hot Core ($d \sim 400$ pc).[8,18] Furthermore, CH_3OH desorbs in laboratory ice experiments at temperatures of 120-130 K.[46] Low CH_3OH rotation temperatures of <20 K have been reported toward low-mass protostars in nearby clouds, with investigators noting rotation temperatures do not necessarily reflect kinetic temperatures.[4,47] As noted in Section 4.3, the GMCs in the present sample are not yet well-characterized, making it difficult to determine whether the kinetic temperatures of the CH_3OH gas are, in fact, much higher than the derived rotation temperatures.

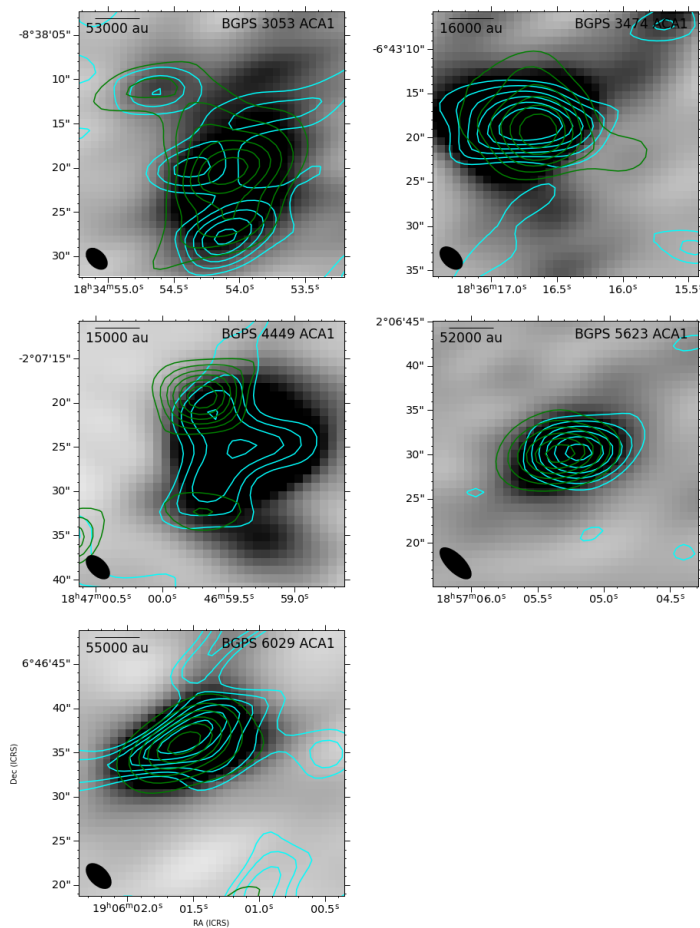Methanol has been detected in prestellar cores, for example,

Fig. 13 Distribution of c-C_3H_2 showed by cyan contours compared to CH_3OH emission (green contours), represented by the integrated intensity (moment 0) maps of the 217.822 and 218.440 GHz lines, respectively. The underlying greyscale images show the Band 6 ($\sim$240 GHz) continuum. The black ellipse in the bottom left of each panel shows the synthesized beam size.

with cold kinetic temperatures of $\sim$10 K in Taurus Molecular Cloud,[21] thus we cannot completely rule out cold kinetic temperatures in our sample of molecular-ring GMCs. If the gas is indeed cold and the derived rotation temperatures of $<$40 K are not the result of beam dilution or discrepancies between excitation and kinetic temperature, a mechanism other than thermal desorption of CH_3OH following formation on icy dust grain mantles is required. One possibility is low-temperature sputtering of CH_3OH off grains by, for example, CO_2, models of which reproduced observed gas-phase CH_3OH abundances in Taurus Molecular Cloud within a factor of 2.5.[48] In addition, grain-grain collisions resulting from turbulence have been offered as an explanation for gas-phase organics in cold regions.[49] X-ray photodesorption of CH_3OH at 15 K in disks has also been demonstrated experimentally.[50] In BGPS 5623 ACA1, BGPS 6029 ACA1, BGPS 6112 ACA1, and BGPS 6120 ACA1, CH_3OH may have been liberated by shocks, which are traced by SiO.

As with temperature, the derived column densities on the order of $\sim$10^{13}–10^{14} cm^{-2} are much lower than those previously detected in hot cores. For example, Bisschop $et\ al.$[8] observed a sample of seven hot cores at distances between 1.0 and 7.7 kpc with the James Clerk Maxwell Telescope and reported CH_3OH column densities on the order of $\sim$10^{16}–10^{18} cm^{-2}. Similarly,

IRAM 30 m observations of Orion KL by Menten $et\ al.$[51] found CH_3OH column densities of $\sim$10^{17} cm^{-2}.

The derived column densities of our sample are more similar to those of 10^{13}–10^{14} cm^{-2} calculated for prestellar cores in Taurus Molecular Cloud.[21] However, as shown in Table 6, all of the CH_3OH emission regions for which column density maps were derived correspond to YSOs or at least YSO candidates, suggesting that these regions are at a more evolved protostellar phase. Instead, it is likely that, as perhaps with rotation temperature, the relatively low derived column densities are the result of beam dilution. As mentioned in Section 4.2, we assumed that the sources in this pilot survey fill the beam. Because these sources are not yet well-characterized, it is difficult to estimate the sizes of individual sources, especially in more complex sources like BGPS 6120 ACA1. However, it is likely that few sources fill the beam, especially in observations of more distant ($d \sim 11$ kpc) GMCs.

If we assume, for example, that the massive YSO corresponding to BGPS 5623 ACA1 (Table 6) has a radius of at most 4000 au (assuming a size similar to the Orion KL hot core, which is 10$''$ at a distance of $\sim$400 pc[34])—or $\sim$0.4$''$ at BGPS 5623's distance $\sim$10.49 kpc—we can estimate that the source fills roughly 0.4% of the ACA synthesized beam. Furthermore, if beam dilution is the cause of the low rotation temperatures calculated for our sample,

the partition function (Q in Equation 2) would be about an order of magnitude greater for temperatures closer to $\sim$150 K. In other words, we expect that the column densities are underestimated by at least three orders of magnitude. If this is indeed the case for all sources, the true beam-dilution-corrected CH_3OH column density is likely closer to $\sim 10^{16}$–10^{17} cm^{-2}. Such values would be on the lower end of, but still on par with, CH_3OH column densities derived for other hot cores, including W33A, a molecular-ring hot core with a CH_3OH column density of 2.0×10^{17} cm^{-2}.[8]

For relatively close GMCs ($d \sim 3$–5 kpc), beam dilution is expected to be considerably less. If we again assume the YSO corresponding to BGPS 4449 ACA1 has a radius of 4000 au, we can assume that it has an angular size of $\sim 1.3''$ at BGPS 4449's distance of 3.03 kpc, which in turn suggests it fills roughly 6.5% of the ACA synthesized beam. Coupled with a higher rotation temperature of $\sim$150 K, the true beam-dilution-corrected CH_3OH column densities for relatively nearby GMCs is likely closer to the $\sim 10^{15}$–10^{16} cm^{-2}, which is indeed lower than that other high-mass star-forming regions in the existing literature. This invites the question of whether star-forming regions in our molecular-ring sample have lower column densities than previously studied (massive) YSOs and suggests that the profile of "typical" high-mass YSOs in which $N_{tot}(CH_3OH) \sim 10^{16}$ cm^{-2} is not necessarily a robust representative of the early stages of massive star formation throughout the galaxy. High-angular resolution observations with the full ALMA are thus needed to determine whether the molecular-ring YSOs are indeed less exceptional in terms of molecular abundance or if the CH_3OH column density profiles from ACA observations suffer from beam dilution.

One of the big questions in astrochemistry is whether the chemical inventories and processes observed are universal across the galaxy. As discussed in Section 1, most of our understanding of chemical processes in star-forming regions comes from the local ISM. However, whether chemistry in the molecular ring is different remains to be seen despite there being some key differences between star-forming regions in the molecular ring versus the local ISM. One difference is that the typical astrochemical laboratories—including Taurus Molecular Cloud and Perseus Molecular Cloud—are low-mass star-forming regions. However, high-mass stars, such as those that form in GMCs perhaps like the ones observed in this pilot study, can severely affect the formation, and thus accompanying chemistry, of neighboring YSOs.[52]

Even if the chemistry in the molecular ring is ultimately the same as what is observed in the local ISM, our current understanding of chemical evolution in the galaxy is limited by small sample sizes. This is especially true for the high-mass star-forming regions, our knowledge of which is observationally biased toward the shortest and rarest evolutionary stages located up to $d \sim 3$ kpc.[53] Therefore, broader surveys are necessary to fully investigate the physical and chemical evolutionary sequences of such stars in a statistically meaningful way.

5.3　Outlook

Dedicated high-resolution follow-up investigations of sources in our sample would not only constrain the nature of these objects

Table 6 Objects corresponding to previously identified YSOs

Identifier	Corresponding YSO(s)
BGPS 3053 ACA1	Embedded protostar[57]
BGPS 3474 ACA1	High-mass,[58] flat-spectrum YSO[59]
BGPS 4449 ACA1	High-mass YSO[33]
BGPS 5623 ACA1	High-mass YSO[40,41]
BGPS 6029 ACA1	High-mass YSO[26,27]
BGPS 6112 ACA1	YSO[31,32]
BGPS 6112 ACA2	Class I YSO candidate[23]
BGPS 6112 ACA3	Class II YSO[23]
BGPS 6120 ACA1	5 YSO candidates[23]
BGPS 6299 ACA1	2 YSO candidates[33]
BGPS 6310 ACA1	YSO-bearing clump[31]

but could help astrochemists better understand chemistry in the molecular ring generally. The number of molecular-ring objects that have been studied in the context of astrochemistry is limited. The massive star-forming region W33A ($d \sim 4$ kpc) is one such region that falls within the molecular ring at a radius of 4.2 kpc from the galactic center based on its celestial coordinates ($\alpha_{J2000} = 18^h14^m39^s.4$　$\delta_{J2000} = -17°52'01''$). For example, McCall et al.[54] reported on gas-phase H_3^+, Dartois et al.[55] observed CH_3OH ice, and Gibb et al.[56] presented the overall ice inventory of W33A. With the resolving power of new facilities, studying these more distant molecular-ring regions, even if not exceptionally molecule-rich, will yield even more astrochemical findings.

Fortunately, the chemical emission for many of the objects presented here corresponds to previously identified YSOs and YSO candidates. Some of these were already discussed in Section 4.2. A comprehensive list, based on a thorough literature search using the SIMBAD database, is given in Table 6. The fact that many of the CH_3OH emission regions presented here correspond to objects that have been, at least preliminarily, characterized in terms of their physical aspects and evolutionary stage emphasizes the potential for these objects to provide new insights about the chemistry alongside (massive) star formation.

6　Conclusions

We present a pilot survey of 11 GMCs selected for their high mass surface density and location in the so-called molecular ring:

1. We identify at least 15 molecular cores with both $C^{18}O$ and fittable CH_3OH emission across 9 (of 11) target GMCs.

2. Rotation temperature and column density maps were derived for regions containing fittable CH_3OH emission. In general, these regions, many of which correspond to previously identified YSOs or YSO candidates, have CH_3OH rotation temperatures of $\leq$20 K and column densities on the order of 10^{13}-10^{14} cm^{-2}. Two GMCs—BGPS 6029 and 6120—have peak derived rotation temperatures of 35–40 K.

3. Silicon- and sulphur-bearing species, possible evidence of shocks propagated by outflows, are found in 10/11 GMCs targeted in this survey. Specifically, SiO is detected in 4/11 GMCs, SO in 10/11, and SO_2 in 2/11. SiO emission in BGPS 5623 and BGPS 6112 may indicate that these clouds contain sources at a different evolutionary stage than other sources in the sample with similar chemical inventories.

4. Some sources harbor multiple YSOs or YSO candidates, some of which are not definitively distinguished in the existing literature. BGPS 4449 ACA1 contains two distinct CH_3OH peaks (not previously reported, to the best of our knowledge), and BGPS 6120 ACA1 contains two or three distinct CH_3OH peaks (and is the site of five YSO candidates, based on previous reports). BGPS 6299 ACA1 is also the site of multiple YSO candidates, according to the existing literature, and it seems to have multiple CH_3OH column density peaks. These sources are especially interesting because they may be targets to study variability in chemical environments within the same physical environment (i.e., a single clump).

The work presented here lays the foundation for follow-up high-angular-resolution studies of the gas-phase chemistry in the molecular ring with ALMA. The variety of tracers identified in the spectra of these sources indicates that these objects contain a rich chemical inventory in which different chemical environments— from shocks propagated by outflows (via SiO) to cold, more diffuse gas (via c-C_3H_2)—can be investigated. Furthermore, investigations of ices in these objects (e.g., with JWST), will help to constrain the coupling between gas and grain chemistry.

Author Contributions

O. H. W. contributed to the conceptualization, investigation, methodology, visualization, and writing the original manuscript draft. G. A. B. contributed to conceptualization, funding acquisition, methodology, and reviewing the prepared manuscript.

Conflicts of interest

There are no conflicts to declare.

Acknowledgements

References

1 E. F. van Dishoeck and G. A. Blake, *Annu. Rev. Astron. Astrophys.*, 1998, **36**, 317–368.

2 E. Herbst and E. F. van Dishoeck, *Annu. Rev. Astron. Astrophys.*, 2009, **47**, 427–480.

3 K. I. Öberg, N. van der Marel, L. E. Kristensen and E. F. van Dishoeck, *Astrophys. J.*, 2011, **740**, 14.

4 K. I. Öberg, T. Lauck and D. Graninger, *Astrophys. J.*, 2014, **788**, 68.

5 G. A. Blake, E. C. Sutton, C. R. Masson and T. G. Phillips, *Astrophys. J.*, 1987, **315**, 621.

6 F. F. S. van der Tak, E. F. van Dishoeck and P. Caselli, *Astron. Astrophys.*, 2000, **361**, 327–339.

7 F. F. S. van der Tak, E. F. van Dishoeck, I. Evans, Neal J. and G. A. Blake, *Astrophys. J.*, 2000, **537**, 283–303.

8 S. E. Bisschop, J. K. Jørgensen, E. F. van Dishoeck and E. B. M. de Wachter, *Astron. Astrophys.*, 2007, **465**, 913–929.

9 N. Z. Scoville and P. M. Solomon, *Astrophys. J. Lett.*, 1975, **199**, L105–L109.

10 D. B. Sanders, P. M. Solomon and N. Z. Scoville, *Astrophys. J.*, 1984, **276**, 182–203.

11 A. J. Battisti and M. H. Heyer, *Astrophys. J.*, 2014, **780**, 173.

12 I. Evans, Neal J., M. M. Dunham, J. K. Jørgensen, M. L. Enoch, B. Merín, E. F. van Dishoeck, J. M. Alcalá, P. C. Myers, K. R. Stapelfeldt, T. L. Huard, L. E. Allen, P. M. Harvey, T. van Kempen, G. A. Blake, D. W. Koerner, L. G. Mundy, D. L. Padgett and A. I. Sargent, *Astrophys. J. Suppl. Ser.*, 2009, **181**, 321–350.

13 H. S. P. Müller, S. Thorwirth, D. A. Roth and G. Winnewisser, *Astron. Astrophys.*, 2001, **370**, L49–L52.

14 H. S. P. Müller, F. Schlöder, J. Stutzki and G. Winnewisser, *J. Mol. Struc.*, 2005, **742**, 215–227.

15 C. P. Endres, S. Schlemmer, P. Schilke, J. Stutzki and H. S. P. Müller, *J. Mol. Spec.*, 2016, **327**, 95–104.

16 Z. Lin, Y. Sun, Y. Xu, J. Yang and Y. Li, *Astrophys. J. Suppl. Ser.*, 2021, **252**, 20.

17 K. I. Öberg, A. C. A. Boogert, K. M. Pontoppidan, S. van den Broek, E. F. van Dishoeck, S. Bottinelli, G. A. Blake and N. J. Evans, *The Astrophysical Journal*, 2011, **740**, 109.

18 O. H. Wilkins, P. B. Carroll and G. A. Blake, *Astrophys. J.*, 2022, **924**, 4.

19 M. Newville, R. Otten, A. Nelson, A. Ingargiola, T. Stensitzki, D. Allan, A. Fox, F. Carter, Michał, D. Pustakhod, Y. Ram, Glenn, C. Deil, Stuermer, A. Beelen, O. Frost, N. Zobrist, G. Pasquevich, A. L. R. Hansen, T. Spillane, S. Caldwell, A. Polloreno, andrewhannum, J. Zimmermann, J. Borreguero, J. Fraine, deep 42-thought, B. F. Maier, B. Gamari and A. Almarza, *lmfit/lmfit-py 0.9.15*, 2019, `https://doi.org/10.5281/zenodo.3567247`.

20 A. Remijan, L. E. Snyder, D. N. Friedel, S. Y. Liu and R. Y. Shah, *Astrophys. J.*, 2003, **590**, 314–332.

21 S. Scibelli and Y. Shirley, *Astrophys. J.*, 2020, **891**, 73.

22 T. P. Ellsworth-Bowers, J. Glenn, A. Riley, E. Rosolowsky, A. Ginsburg, I. Evans, Neal J., J. Bally, C. Battersby, Y. L. Shirley and M. Merello, *Astrophys. J.*, 2015, **805**, 157.

23 G. Saral, J. L. Hora, S. E. Willis, X. P. Koenig, R. A. Gutermuth and A. T. Saygac, *Astrophys. J.*, 2015, **813**, 25.

24 H. Beuther, P. Schilke, K. M. Menten, F. Motte, T. K. Sridharan and F. Wyrowski, *Astrophys. J.*, 2002, **566**, 945–965.

25 X. Lu, Q. Zhang, H. B. Liu, J. Wang and Q. Gu, *Astrophys. J.*, 2014, **790**, 84.

26 B. E. Svoboda, Y. L. Shirley, C. Battersby, E. W. Rosolowsky, A. G. Ginsburg, T. P. Ellsworth-Bowers, M. R. Pestalozzi, M. K. Dunham, I. Evans, Neal J., J. Bally and J. Glenn, *Astrophys. J.*, 2016, **822**, 59.

27 M. B. Areal, S. Paron, M. Celis Peña and M. E. Ortega, *Astron. Astrophys.*, 2018, **612**, A117.

28 F. Fontani, T. Sakai, K. Furuya, N. Sakai, Y. Aikawa and S. Yamamoto, *Mon. Not. R. Astron. Soc.*, 2014, **440**, 448–456.

29 F. Fontani, G. Busquet, A. Palau, P. Caselli, Á. Sánchez-Monge, J. C. Tan and M. Audard, *Astron. Astrophys.*, 2015, **575**, A87.

30 E. F. E. Morales, F. Wyrowski, F. Schuller and K. M. Menten, *Astron. Astrophys.*, 2013, **560**, A76.

31 J. S. Urquhart, C. König, A. Giannetti, S. Leurini, T. J. T. Moore, D. J. Eden, T. Pillai, M. A. Thompson, C. Braiding, M. G. Burton, T. Csengeri, J. T. Dempsey, C. Figura, D. Froebrich, K. M. Menten, F. Schuller, M. D. Smith and F. Wyrowski, *Mon. Not. R. Astron. Soc.*, 2018, **473**, 1059–1102.

32 J. S. Urquhart, T. Csengeri, F. Wyrowski, F. Schuller, S. Bontemps, L. Bronfman, K. M. Menten, C. M. Walmsley, Y. Contreras, H. Beuther, M. Wienen and H. Linz, *Astron. Astrophys.*, 2014, **568**, A41.

33 G. Saral, J. L. Hora, M. Audard, X. P. Koenig, J. R. Martínez-Galarza, F. Motte, Q. Nguyen-Luong, A. T. Saygac and H. A. Smith, *Astrophys. J.*, 2017, **839**, 108.

34 N. R. Crockett, E. A. Bergin, J. L. Neill, C. Favre, P. Schilke, D. C. Lis, T. A. Bell, G. Blake, J. Cernicharo, M. Emprechtinger, G. B. Esplugues, H. Gupta, M. Kleshcheva, S. Lord, N. Marcelino, B. A. McGuire, J. Pearson, T. G. Phillips, R. Plume, F. van der Tak, B. Tercero and S. Yu, *Astrophys. J.*, 2014, **787**, 112.

35 J. Martin-Pintado, R. Bachiller and A. Fuente, *Astron. Astrophys.*, 1992, **254**, 315–326.

36 P. Schilke, C. M. Walmsley, G. Pineau des Forets and D. R. Flower, *Astron. Astrophys.*, 1997, **321**, 293–304.

37 I. Jiménez-Serra, P. Caselli, J. Martín-Pintado and T. W. Hartquist, *Astron. Astrophys.*, 2008, **482**, 549–559.

38 I. Jiménez-Serra, J. Martín-Pintado, A. Rodríguez-Franco and S. Martín, *Astrophys. J. Lett.*, 2005, **627**, L121–L124.

39 I. Jiménez-Serra, J. Martín-Pintado, P. Caselli, S. Viti and A. Rodríguez-Franco, *Astrophys. J.*, 2009, **695**, 149–155.

40 J. M. Rathborne, J. M. Jackson and R. Simon, *Astrophys. J.*, 2006, **641**, 389–405.

41 Q. Nguyen Luong, F. Motte, M. Hennemann, T. Hill, K. L. J. Rygl, N. Schneider, S. Bontemps, A. Men'shchikov, P. André, N. Peretto, L. D. Anderson, D. Arzoumanian, L. Deharveng, P. Didelon, J. di Francesco, M. J. Griffin, J. M. Kirk, V. Könyves, P. G. Martin, A. Maury, V. Minier, S. Molinari, M. Pestalozzi, S. Pezzuto, M. Reid, H. Roussel, M. Sauvage, F. Schuller, L. Testi, D. Ward-Thompson, G. J. White and A. Zavagno, *Astron. Astrophys.*, 2011, **535**, A76.

42 J. M. Vrtilek, C. A. Gottlieb and P. Thaddeus, *Astrophys. J.*, 1987, **314**, 716.

43 Y. Lin, S. Spezzano, O. Sipilä, A. Vasyunin and P. Caselli, *Astron. Astrophys.*, 2022, **665**, A131.

44 K. G. Johnston, D. S. Shepherd, T. P. Robitaille and K. Wood, *Astron. Astrophys.*, 2013, **551**, A43.

45 L. Moscadelli, M. J. Reid, K. M. Menten, A. Brunthaler, X. W. Zheng and Y. Xu, *Astrophys. J.*, 2009, **693**, 406–412.

46 K. I. Öberg, R. T. Garrod, E. F. van Dishoeck and H. Linnartz, *Astron. Astrophys.*, 2009, **504**, 891–913.

47 D. M. Graninger, O. H. Wilkins and K. I. Öberg, *Astrophys. J.*, 2016, **819**, 140.

48 A. Paulive, J. T. Carder and E. Herbst, *Mon. Not. R. Astron. Soc.*, 2022, **516**, 4097–4110.

49 J. Kalvāns and K. Silsbee, *Mon. Not. R. Astron. Soc.*, 2022, **515**, 785–794.

50 R. Basalgète, R. Dupuy, G. Féraud, C. Romanzin, L. Philippe, X. Michaut, J. Michoud, L. Amiaud, A. Lafosse, J. H. Fillion and M. Bertin, *Astron. Astrophys.*, 2021, **647**, A35.

51 K. M. Menten, C. M. Walmsley, C. Henkel and T. L. Wilson, *Astron. Astrophys.*, 1988, **198**, 253–266.

52 C. J. Lada and E. A. Lada, *Annu. Rev. Astron. Astrophys.*, 2003, **41**, 57–115.

53 F. Motte, S. Bontemps and F. Louvet, *Annu. Rev. Astron. Astrophys.*, 2018, **56**, 41–82.

54 B. J. McCall, T. R. Geballe, K. H. Hinkle and T. Oka, *Astrophys. J.*, 1999, **522**, 338–348.

55 E. Dartois, W. Schutte, T. R. Geballe, K. Demyk, P. Ehrenfreund and L. D'Hendecourt, *Astron. Astrophys.*, 1999, **342**, L32–L35.

56 E. L. Gibb, D. C. B. Whittet, W. A. Schutte, A. C. A. Boogert, J. E. Chiar, P. Ehrenfreund, P. A. Gerakines, J. V. Keane, A. G. G. M. Tielens, E. F. van Dishoeck and O. Kerkhof, *Astrophys. J.*, 2000, **536**, 347–356.

57 S. E. Ragan, E. A. Bergin and R. A. Gutermuth, *Astrophys. J.*, 2009, **698**, 324–349.

58 M. Wienen, F. Wyrowski, F. Schuller, K. M. Menten, C. M. Walmsley, L. Bronfman and F. Motte, *Astron. Astrophys.*, 2012, **544**, A146.

59 T. Baug, L. K. Dewangan, D. K. Ojha and J. P. Ninan, *Astrophys. J.*, 2016, **833**, 85.

60 M. Wenger, F. Ochsenbein, D. Egret, P. Dubois, F. Bonnarel, S. Borde, F. Genova, G. Jasniewicz, S. Laloë, S. Lesteven and R. Monier, *Astron. Astrophys. Suppl. Ser.*, 2000, **143**, 9–22.

61 T. Robitaille and E. Bressert, *APLpy: Astronomical Plotting Library in Python*, Astrophysics Source Code Library, 2012.

62 T. Robitaille, *APLpy v2.0: The Astronomical Plotting Library in Python*, 2019, `https://doi.org/10.5281/zenodo.2567476`.